



ELSEVIER

Contents lists available at [SciVerse ScienceDirect](http://www.sciencedirect.com)

Earth and Planetary Science Letters

journal homepage: www.elsevier.com/locate/epsl

Electromagnetic detection of plate hydration due to bending faults at the Middle America Trench

Kerry Key^{a,*}, Steven Constable^a, Tetsuo Matsuno^{b,1}, Rob L. Evans^b, David Myer^{a,2}^a Scripps Institution of Oceanography, University of California San Diego, La Jolla, CA, USA^b Department of Geology and Geophysics, Woods Hole Oceanographic Institution, Woods Hole, MA, USA

ARTICLE INFO

Article history:

Received 23 January 2012

Received in revised form

7 July 2012

Accepted 16 July 2012

Editor: Y. Ricard

Available online 29 August 2012

Keywords:

subduction zones
marine geophysics
electromagnetics
conductivity

ABSTRACT

Water plays an important role in the processes occurring at subduction zones since the release of water from the downgoing slab impacts seismicity and enhances arc volcanism. Geochemical indicators suggest that the Nicaraguan slab is anomalously wet, yet the mechanism of slab hydration remains poorly constrained. Extensional bending faults on the incoming oceanic plate of the Middle America Trench offshore Nicaragua have been observed to penetrate to mantle depths, suggesting a permeable pathway for hydration of the crust and serpentinization of the upper mantle. Low seismic velocities observed in the uppermost mantle of the incoming plate have been explained as serpentinization due to deep fluid penetration but could also be explained by intrinsic anisotropy and fractures in the absence of fluid circulation. Here we use controlled-source electromagnetic imaging to map the electrical resistivity of the crust and uppermost mantle along a 220 km profile crossing the trench offshore Nicaragua. Along the incoming plate our data reveal that crustal resistivity decreases by up to a factor of five directly with the onset of the bending faults. Furthermore, a strong azimuthal anisotropy compatible with conductive vertical fault planes is observed only on the faulted trench seafloor. The observed resistivity decrease and anisotropy can be explained by a porosity increase along vertical fault planes, which we interpret as evidence that the lithospheric bending faults provide the necessary permeable fluid pathways required for serpentinization of the uppermost mantle. This implies that most serpentinisation happens at the trench, with the width of the faulting region and the density of fractures controlling the extent of upper mantle alteration. This observation explains why the heavily faulted trench offshore Nicaragua is associated with an anomalously wet slab, whereas other sections of the Middle America Trench containing fewer bending faults have less fluid flux from the subducting slab.

© 2012 Elsevier B.V. All rights reserved.

1. Introduction

At the Middle America Trench offshore Nicaragua, the incoming Cocos plate experiences flexural bending prior to its subduction beneath Central America. Extensional forces associated with the bending reactivate normal faults that were originally formed during plate genesis at the mid-ocean ridge, as well as creating new fractures, resulting in a heavily faulted seafloor on the trench outer rise wall (Masson, 1991; Alexander and Macdonald, 1996). Seismic reflection images show that the extensive network of trench parallel normal faults penetrates the entire oceanic crust

and at least 10 km into the mantle (Ranero et al., 2003). This pervasive fracturing is thought to promote seawater intrusion through the crust and into the uppermost mantle where water serpentinizes peridotite (Ranero et al., 2003; Faccenda et al., 2009). Since this mineral bound water is subducted with the down-going slab where its eventual release at depth affects intraplate seismicity and increases arc magmatism, knowledge of the volume of water being carried into the mantle through this process is crucial for understanding the factors controlling the subduction system (Peacock, 1990).

Geochemical sampling of lavas from the Central American arc shows unusually high element and isotope ratios in Nicaragua that can be explained by a strong slab component of fluid flux, suggesting that the Nicaraguan slab is anomalously wet (Carr et al., 2003; Rupke et al., 2002; Abers et al., 2003). This onshore evidence is complemented by marine geophysical studies in the Middle America Trench that are compatible with plate hydration due to the bending faults. Seafloor heat flow decreases

* Corresponding author.

E-mail address: kkey@ucsd.edu (K. Key).URL: <http://marineemlab.ucsd.edu/kkey> (K. Key).¹ Now at Department of Earth and Planetary Sciences, Kobe University, Kobe, Japan.² Now at BlueGreen Geophysics LLC, Encinitas, CA, USA.

systematically with both proximity to the trench and increasing fault density, suggesting enhanced hydrothermal circulation and cooling within the fault complex (Grevemeyer et al., 2005). Slow seismic velocities observed beneath the trench outer rise have been explained as 15–30% serpentinization of the uppermost mantle to depths of at least a few kilometers beneath the Moho (Grevemeyer et al., 2007; Ivandic et al., 2008, 2010; van Avendonk et al., 2011). However, alternative explanations for the slow velocities include anisotropic effects and weakening due to fracturing, both of which do not require the deep hydration and alteration of mantle olivine into serpentine (Ivandic et al., 2010; van Avendonk et al., 2011), and therefore would predict lower volumes of water in the down-going slab.

While these lines of evidence imply plate hydration at the shallow and deep scales, an essential missing link has been data that can constrain the degree to which pore fluids are present within the faulted crust. Furthermore, there are few constraints on the volumes of water that may exit the system through hydrofracturing of the upper plate at relatively shallow depths beneath the margin (Ranero et al., 2008). For this reason, we carried out a large-scale electromagnetic survey to characterize the electrical structure, and hence porosity, of the crust and upper mantle in this region (Fig. 1).

Electrical resistivity is a physical property that depends on the presence of fluids, particularly at crustal depths where the bulk resistivity is predominantly controlled by conductive pore water and the degree of porosity and its connectivity. Our 220 km long survey profile spans from the abyssal plain, across the trench and up the margin slope onto the continental shelf, allowing us to map the variation of fluid circulation with distance from the trench and therefore with the degree of plate bending and fracturing, and to characterize the dewatering processes and fracturing occurring beneath the margin slope.

A previous electromagnetic survey using the passive magnetotelluric method has been conducted to the south offshore Costa Rica, where the low frequencies of magnetotelluric data provided constraints on deeper and broader scale features of the subduction zone fluid cycle (Worzewski et al., 2010). For the shallower

lithospheric imaging focus of our project, we applied the controlled-source electromagnetic (CSEM) method, where a deep-towed electric dipole transmits higher frequency electromagnetic energy through the seabed to an array of seafloor EM recorders that measure the resulting attenuation and phase shift of the induced electric and magnetic fields. Moreover, CSEM data are better suited for constraining electrical anisotropy associated with faulting (Yu et al., 1997; Everett and Constable, 1999). While CSEM technology was originally invented over three decades ago to measure the high resistivity of the abyssal plain lithosphere and the oceanic crust at mid-ocean ridges (Cox, 1981), recognition of its utility for mapping resistive hydrocarbon reservoirs on the sedimented continental shelves has led to significant improvements in data acquisition and interpretation during the past decade (Key, 2012). Our survey is the first to use the CSEM method to study a subduction zone and leveraged several technological advances resulting from this recent industrial activity.

2. Marine CSEM experiment

We collected the CSEM data during a month long research cruise on the R/V Melville in April–May 2010 as part of the Serpentinite, Extension and Regional Porosity Experiment across the Nicaraguan Trench (SERPENT). The main data set consists of CSEM soundings recorded by an array of 44 seafloor EM receivers deployed along the 220 km survey profile (Fig. 1). We augmented the CSEM data with two stations of highly sensitive long-wire electromagnetic (LEM) data that measured the azimuthal dependence of the electric fields generated during circular transmitter tows of 30 km radius around each station (Fig. 1). A reference LEM circle on the unfaulted abyssal plain was designed to measure any electrical anisotropy frozen in during lithospheric formation at the mid-ocean ridge, while a second LEM circle on the trench outer rise targeted further anisotropy created by the fault structures and any associated upper mantle serpentinization. An additional data set of broadband magnetotelluric recordings from each EM receiver constrains deeper asthenosphere conductivity and will be presented elsewhere. The remainder of this section describes the acquisition in more detail for the interested reader, but could be skipped by non-specialists.

The seafloor CSEM consisted of broadband EM receivers that measure the horizontal electric and magnetic field variations in the 0.0001–100 Hz frequency band (Constable et al., 1998). The receiver positions on the seafloor were determined using long-baseline navigation from the survey vessel, which yielded horizontal position uncertainties in the range of 1–50 m, depending on water depth and the acoustic data coverage. Because the receivers are freely deployed to the seafloor where they land with an arbitrary rotation, external electronic compass recorders are required to measure their orientations. We performed an independent verification of the compass orientations by using a method that simultaneously inverts for the seafloor resistivity and the optimal rotation matrix between the observed data and the response predicted by the resistivity model (Key and Lockwood, 2010), finding agreement with all compass orientations to within 8° uncertainty.

The CSEM transmissions were accomplished using the Scripps Undersea EM Source Instrument (SUESI). SUESI transmitted a 300 A current across copper electrodes attached to each end of a 250 m long antenna, resulting in a dipole moment of 75 kA m. We deep-towed SUESI across the trench at a tow speed of 1.5 kts (0.8 m/s) for the 220 km long profile. A nominal 100 m altitude was maintained to ensure good EM coupling to the seafloor while leaving a margin of safety above the rugged topography (Fig. 2a). An external sensor mounted on SUESI's tow-frame recorded

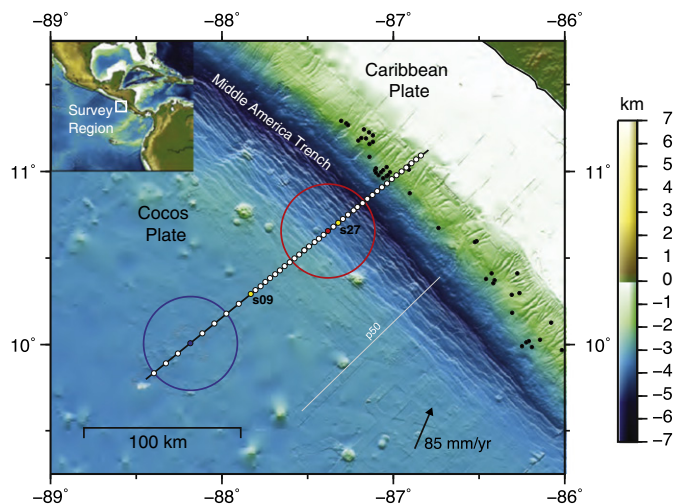


Fig. 1. Marine EM survey across the Middle America trench offshore Nicaragua. Seafloor EM receivers (colored dots) and the deep-towed EM transmitter tow path (black line) extend from the unfaulted abyssal plain, across the heavily faulted trench outer rise, and up the continental margin slope. Data from receivers s09 and s27 (yellow dots) are shown in Fig. 3. Blue and red dots denote the location of the LEM sensors used to detect anisotropy with circular transmitter tows (large blue and red circles). Black dots show the location of known seafloor fluid seeps (Sahling et al., 2008). The grey line shows seismic refraction profile p50 (Ivandic et al., 2008). The arrow indicates the present day plate motion of the incoming Cocos plate with respect to the overriding Caribbean plate (DeMets, 2001).

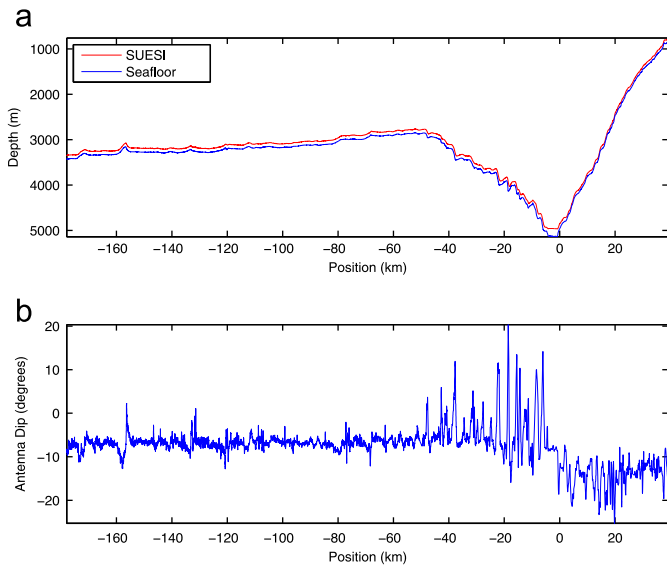


Fig. 2. (a) Depth of the Scripps Undersea EM Source Instrument (SUESI) and the seafloor depth during the deep-tow across the Middle America Trench offshore Nicaragua. SUESI's target altitude during the deep-tow was 100 m above the seafloor. (b) Dip of SUESI's 250 m long dipole antenna (negative corresponds to the front electrode being shallower than the tail electrode). The largest dip variations occur in the trench outer rise where the transmitter was rapidly raised and lowered over the heavily faulted seafloor.

seawater conductivity, temperature, pressure depth, and sound velocity data. SUESI's height above the seafloor was measured by an acoustic altimeter. Depth recordings from a pressure sensor attached to the trailing electrode allowed us to compute the dip angle of the dipole antenna (Fig. 2b). Over the abyssal plain the antenna dip is fairly stable at a nominal value of about -7° (negative corresponds to the front electrode being shallower than the tail electrode). At the trench outer rise there are several relatively short excursions to 0 – 20° dip that occurred when the transmitter was lowered deeper after crossing over down-dropping fault scarps. The dip changes to negative values in the range of -10° to -20° when SUESI was raised to shallower depths while towing up the margin slope.

The transmitted current was switched using a compact binary waveform referred to as Waveform D (Myer et al., 2011). The discrete frequency spectrum of this waveform is advantageous since its peak harmonics are spread out across the spectrum in a wider band than is possible with the simple square waves used in older generations of marine CSEM experiments. Based on pre-survey forward modeling of the 500 m of conductive porous sediments overlying resistive volcanic seafloor, we determined that a waveform fundamental frequency of 0.25 Hz (with peak harmonics at 0.75 and 1.75 Hz) would provide high sensitivity to crustal structure while maintaining a good signal-to-noise ratio. Phase stability of the transmitted waveform was maintained by a 400 Hz GPS locked timing signal transmitted down the deep-tow cable to the source.

SUESI's lateral position was determined using an inverted long-baseline (ILBL) navigation system. The ILBL system records the acoustic travel times between an acoustic transceiver mounted on SUESI and two GPS-equipped acoustic transponders towed on the sea-surface behind the ship. Paravanes were used to position the surface transponders to the port and starboard sides approximately 100 m behind the ship, resulting in a 300 m aperture between the transponders. The acoustic travel times, the GPS positions of the transponders and the measured transmitter depth were then input into a Levenberg–Marquardt minimization routine that solved for SUESI's lateral position by ray-

tracing through the seawater sound velocity profile. Estimated SUESI position uncertainties from the ILBL system are about 10 m in the tow direction and 100–200 m in the cross-line direction for the deepwater (> 2500 m depth), and are much smaller at the shallower depths encountered on the margin slope.

The LEM receivers were used to measure azimuthal anisotropy in the crust and uppermost mantle by towing the transmitter in a 30 km radius circle around a vector pair of LEMs (Supplemental Fig. S1). Each LEM receiver was outfitted with a 200 m long antenna for measuring the horizontal electric field at a much lower noise level than possible with the 10 m dipoles used on the standard CSEM receivers (Constable and Cox, 1996). This improved sensitivity comes at the cost of a much longer time to deploy the LEM since the long antenna requires a careful deep-tow deployment to the seafloor. Since each LEM only measures a single component of the electric field, orthogonal pairs of LEMs deployed at the center of each anisotropy circle comprise a complete LEM station.

3. Data and results

3.1. CSEM data

We processed the CSEM data using a short-time window, robust stacking method (Myer et al., 2011). This entailed dividing the time series for each channel into 4 s time-windows corresponding to the fundamental period of the transmitter waveform, pre-whitening, Fourier transformation, and then post-darkening the resulting Fourier coefficients. These were then corrected for the frequency dependent sensor responses and the complex transmitter dipole moment. The Fourier coefficients of the first, third and seventh waveform harmonics (0.25, 0.75 and 1.75 Hz) were then stacked into 120 s stacks. We used a robust stacking method that iteratively removed outliers identified as residuals greater than twice the median absolute deviation. Finally, the variance of each stacked value was obtained by analysis of the stacking residuals after removing the small trend due to the changing transmitter range over the 120 s stack window. Data from all receivers are displayed in Supplemental Figs. S2 and S3.

Fig. 3 shows example CSEM responses obtained for the inline electric and crossline magnetic fields measured at sites s09 and s27. The response amplitudes decay rapidly with range from the transmitter due to a combination of geometric spreading and inductive attenuation. At site s09, which is located on the unfaulted abyssal plain, the phases fall off rapidly at short ranges due to inductive attenuation in the conductive seafloor sediments, but then reach a nearly constant phase at ranges greater than 2 km. Constant phases are characteristic of very resistive media that allow the EM energy to propagate with little inductive attenuation. In very shallow water CSEM surveys (< 500 m) this occurs due to EM propagation through the resistive air, whereas here in the deepwater this arises from the high resistivity of the underlying oceanic crust and mantle. While the amplitude responses at s27 appear similar to s09, the phase responses are markedly different, exhibiting increasing phase shifts to offsets of 5–10 km. This is likely due to inductive attenuation associated with the less resistive oceanic crust on the highly faulted trench outer rise, and highlights the importance of including phase data in CSEM interpretations. The phase data on s27 also exhibit short-wavelength variations, particularly evident in the out-tow data; these second order features arise from variations in electromagnetic coupling to the seafloor when the transmitter passed over the rugged fault scarps.

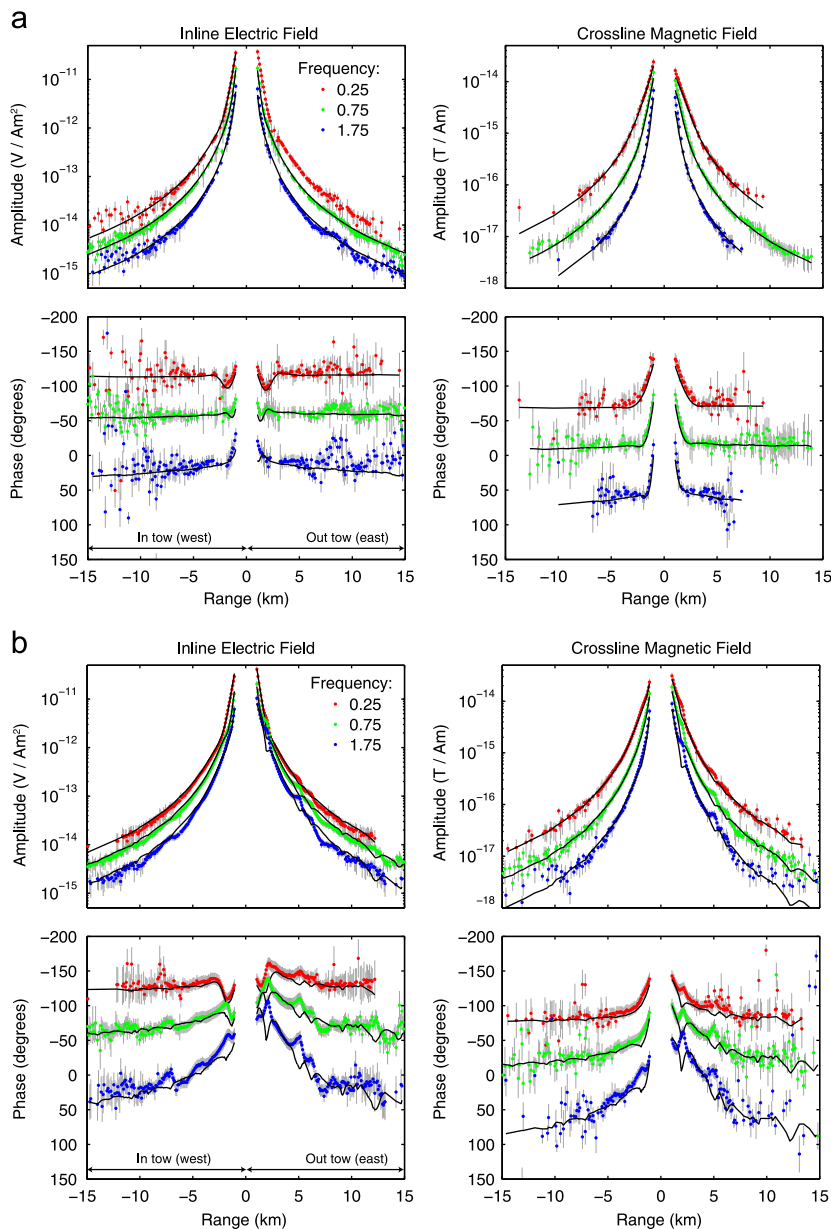


Fig. 3. Example CSEM responses from sites s09 (a) and s27 (b). Electric and magnetic fields amplitude and phase responses (dots) are shown as a function of source-receiver offset for three strongest harmonics of the source waveform. Site s27 shows a stronger phase shift as a function of range that is indicative of a decrease in crustal resistivity over the heavily faulted seafloor. Model fits for separate 1D inversions of the in- and out-tow data are shown as black lines. Data standard errors are shown as light gray bars. The locations of s09 and s27 are shown in Fig. 1.

Fig. 4 shows the electric field data at 0.75 Hz for all receivers. There are distinct lateral variations in the amplitude and phase responses across the profile, with the largest changes occurring at the transition from the oceanic plate to the continental margin at 0 km position. There is a more subtle transition in the data as the array crosses the trench. Due to the increased seafloor conductivity on the margin slope, the phase data here vary most rapidly as a function of range.

3.2. CSEM resistivity results

We divided the CSEM data from each receiver into in-tow and out-tow subsets and then inverted each for a 1D seafloor resistivity model using an open-source inversion algorithm (Key, 2009). Due to the inline geometry, the CSEM data are primarily sensitive to conductivity in the vertical plane of the survey profile

and are insensitive to the azimuthal anisotropy that may be present from the faulting. Hence we inverted only for isotropic resistivity. An error floor of 15% was applied to the data uncertainties and only data with signal-to-noise ratios greater than two were inverted. Because data at the shortest offsets are predominantly sensitive only to the seawater conductivity and are also highly susceptible to bias from uncertainties in the transmitter and receiver position estimates, we omitted data at ranges less than 1 km. All inversions were started from a uniform 100 ohm m halfspace starting model and were stabilized using a vertical model roughness penalty term in the regularization functional (Constable et al., 1987). Most of the inversions were able to fit the data to RMS 1.0. The resulting 1D inversion models were collated into a 2D image that shows the variations in resistivity along the survey profile (Fig. 5a). The corresponding model fits for all data are shown in Supplemental Figs. S2 and S3.

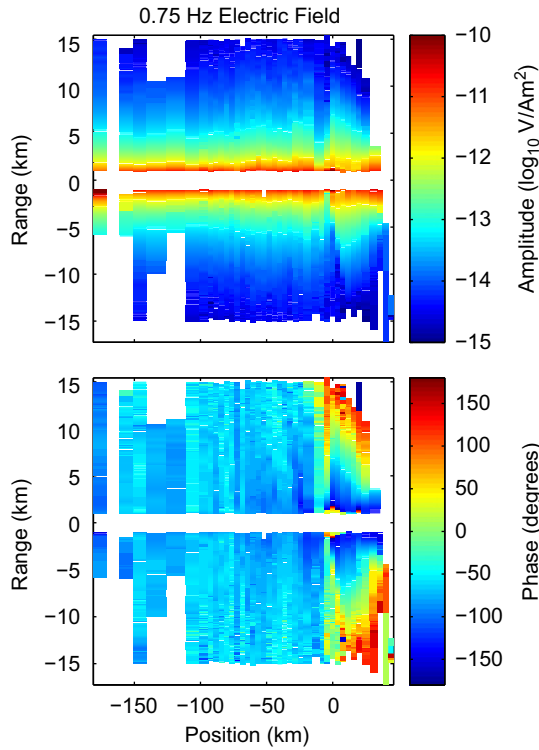


Fig. 4. In-line electric field data at 0.75 Hz shown as amplitude (top) and phase (bottom). Negative ranges correspond to the in-tow data (transmitter located to the west of the receiver) while positive ranges correspond to out-tow data (transmitter located to the east of the receiver).

The oceanic plate resistivity varies predominantly in the vertical direction, starting with about 500 m of conductive 1 ohm m sediments and increasing to 1000 ohm m or greater within a few kilometers depth (Fig. 5a). The vertical resistivity gradient agrees well with crustal boundaries identified by seismic imaging (Grevemeyer et al., 2007). The 2 km of extrusive pillow basalts and sheeted dikes in seismic layer 2 are characterized by resistivities of 10–100 ohm m while the deeper intrusive gabbros of layer 3 are generally much greater than 100 ohm m.

Resolution analyses for EM data are notoriously difficult due to the non-linearity of the inverse problem. However, we can test for the depth of maximum inference (Parker, 1982) by inverting each data set after placing a highly conductive (10^{-6} ohm m) layer at the base of the model. The top of this conductive layer was iteratively moved to shallower depths until the inversions could no longer obtain RMS 1.0. This depth was then taken to be the depth of maximum inference, below which the CSEM data are unable to constrain the resistivity structure. The depth of maximum inference was found to be about 7–8 km beneath the seafloor, corresponding to the uppermost few kilometers of the mantle.

Since the large vertical resistivity gradient in the oceanic plate obscures more subtle lateral variations, we normalized the resistivity model by a vertical profile obtained by averaging all stations on the oceanic plate. This reveals that a prominent lateral drop in crustal resistivity occurs directly with the onset of the bending faults on the outer rise (Fig. 5b). Here the resistivity decreases by up to a factor of 5 at depths spanning the entire crust and possibly deeper, although the precise bottom to this region is not well-constrained by the CSEM data. This decreased resistivity lies directly over the region where low seismic velocities suggest upper mantle serpentinization (Ivandic et al., 2008; van Avendonk et al., 2011).

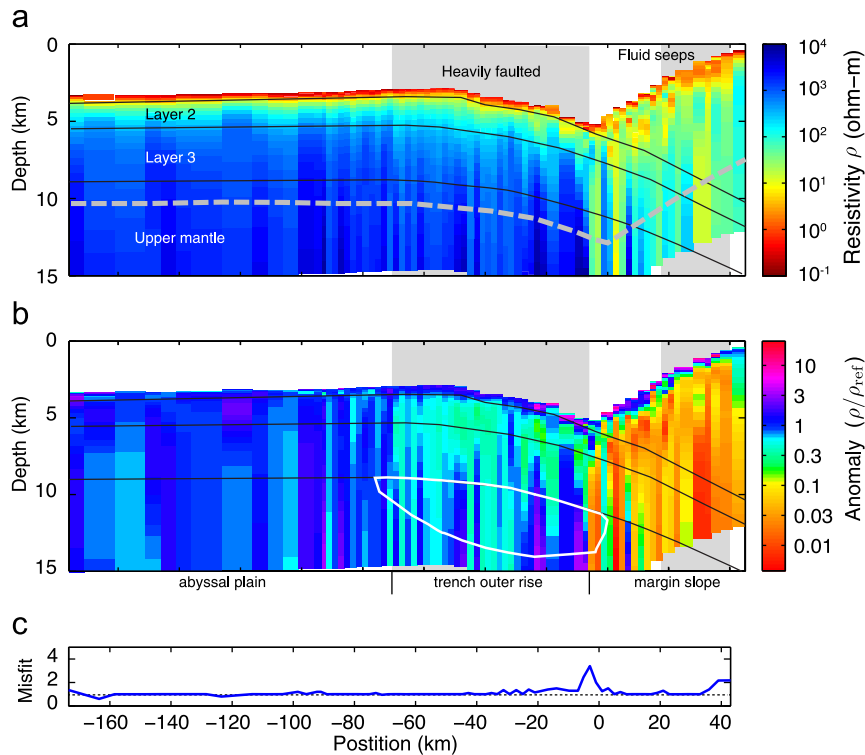


Fig. 5. (a) Resistivity section obtained from 1D inversion of the data from each receiver. Black lines show crustal layering determined from active source seismic studies (Grevemeyer et al., 2007). The dashed line shows the maximum depth of inference. Vertical exaggeration is $5 \times$. (b) Lateral resistivity variations are accentuated by plotting the ratio of the observed resistivity to a reference vertical profile obtained from the average of all sites at positions -173 to -80 km. The white line encloses a region of low mantle velocities detected by seismic refraction data collected along profile p50 (Ivandic et al., 2008). (c) RMS misfit for each site's 1D inversion.

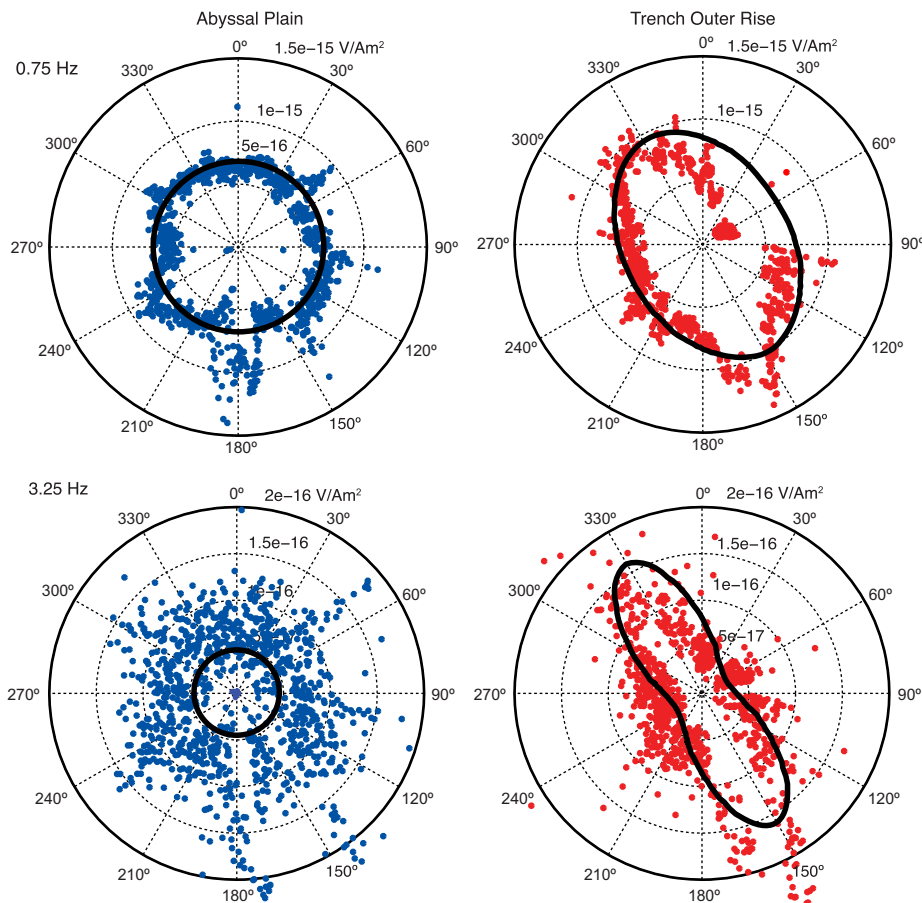


Fig. 6. Electromagnetic polarization ellipse maxima shown as a function of transmitter azimuth for the 0.75 Hz (top) and 3.25 Hz (bottom) LEM circle data. A fault parallel anisotropy is evident in the elongation of the trench outer-rise data, whereas the abyssal plain data show a predominantly circular polarization that is expected when anisotropy is insignificant. Solid black lines show model responses for an isotropic resistive crust beneath the abyssal plain, and an anisotropic crust beneath the trench outer rise with a factor of 5 decrease in resistivity in the vertical and trench parallel directions, representative of conductive vertical fault planes.

3.3. Long-wire EM data and results

We processed the LEM data in an identical manner as the CSEM data and then transformed them into electromagnetic polarization ellipse parameters as a function of source-receiver azimuth (e.g., Behrens, 2005). The maxima of the polarization ellipses for the 0.75 and 3.25 Hz harmonics are shown in Fig. 6. On the abyssal plain, the polarization maxima show an isotropic response as a function of transmitter azimuth. Conversely, the trench outer rise polarization maxima are highly elongated in a fault parallel direction. Since the electric field becomes enhanced in the conductive direction of anisotropic structures (Everett and Constable, 1999), these data indicate that the fault parallel direction is the most conductive.

We forward modeled the LEM data by modifying a 2D finite element code (Key and Oval, 2011) to handle a triaxial electrical resistivity tensor $\bar{\rho}$ of the form:

$$\bar{\rho} = \begin{bmatrix} \rho_x & 0 & 0 \\ 0 & \rho_y & 0 \\ 0 & 0 & \rho_z \end{bmatrix} \quad (1)$$

where ρ_x , ρ_y , and ρ_z are the resistivities along the three coordinate axes. Based on the CSEM inversions shown in Fig. 5a, a simple two layer model was used for the LEM data, consisting of a 500 m thick layer of conductive sediments overlying a resistive anisotropic crust. Table 1 lists the parameters used to generate the fits shown in Fig. 6. The abyssal plain data are well described by an

Table 1

Model parameters used for forward modeling the LEM data shown in Fig. 6. The two layer model consists of 500 m of conductive isotropic sediments overlying a resistive anisotropic crust. For the trench outer rise model, the x-axis is aligned roughly trench and fault parallel at -30° .

| Layer | Abyssal plain | Trench outer rise |
|-------------------|-----------------------------------|--|
| Sediments (ohm m) | 1 | 2.2 |
| Crust (ohm m) | $\rho_x = \rho_y = \rho_z = 3000$ | $\rho_x = \rho_z = 600, \rho_y = 3000$ |

isotropic resistive crust. For the trench outer rise data, a reasonable fit was obtained with the x- and z-axes a factor of five times more conductive than the y-axis, with x aligned at -30° from N, roughly parallel to the trench axis and fault planes. When the x and z resistivities are equal and more conductive than the y-axis, the tensor represents conductive vertical sheets (with strike direction x) embedded in a resistive matrix (Everett and Constable, 1999); this is consistent with an interpretation of the bending faults as trench parallel bands of highly porous fault damage zones extending throughout the entire crust. The factor of five anisotropy agrees with the similar reduction in resistivity constrained by the CSEM data at the trench outer rise (Fig. 5b).

4. Implications for plate hydration

Our observations of oceanic plate resistivity agree in the upper 1 km with CSEM results from 40 Ma lithosphere in the north-east

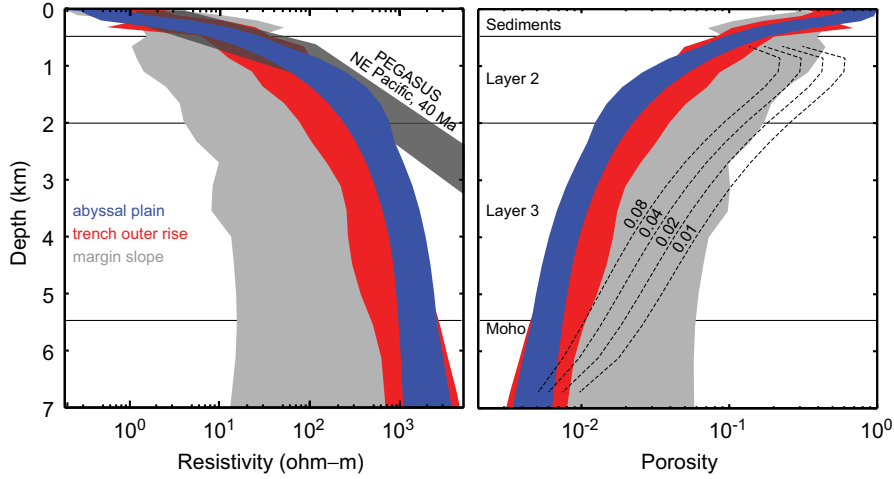


Fig. 7. Left: The range of resistivity observed for all sites located on the abyssal plain (blue), the trench outer rise (red) and the margin slope (light gray). For comparison, the oceanic plate resistivity obtained from LEM data collected on 40 Ma north-east Pacific lithosphere as part of the PEGASUS project is shown in dark gray (Constable and Cox, 1996). Horizontal black lines show crustal layering of the oceanic plate observed by active source seismic studies (Grevemeyer et al., 2007). Right: bulk porosity predicted from resistivity. Thin dashed lines show the estimated fault damage zone porosities for various width to spacing ratios x .

Pacific (Constable and Cox, 1996), but are significantly less resistive at depth (Fig. 7). Since crustal resistivity away from magmatic areas is predominantly controlled by porosity, this disagreement reflects an overall higher porosity in the 22–24 Ma oceanic crust offshore Nicaragua, even on the abyssal plain where there is a little evidence for reactivated normal faults.

The bulk resistivity ρ determined from the CSEM inversions can be related to bulk porosity using Archie's (1942) law:

$$\rho = \rho_w \phi^{-m}, \quad (2)$$

where ϕ is porosity and ρ_w is the saturated fluid resistivity. While this empirical formula was originally derived from well-logs of porous sediments, it is also effective for characterizing conductive pore fluids in crystalline rocks (Brace and Orange, 1968). A value of 2 for the exponent m has been constrained through laboratory studies of basement rocks and well-logging of the sheeted dikes in ODP Hole 504B (Brace and Orange, 1968; Shankland and Waff, 1974; Becker et al., 1982; Becker, 1985). If faulting results in an even more well-connected porosity structure than represented by Archie's law, the exponent m will be smaller and so will the corresponding porosity estimates derived from the CSEM resistivity.

Assuming pore fluids with seawater salinity, the fluid resistivity in the range of 0–200 C can be approximated to 5% accuracy by (Becker et al., 1982):

$$\rho_w(T) = \left(3 + \frac{T}{10}\right)^{-1}, \quad (3)$$

where T is the temperature ($^{\circ}\text{C}$). For our porosity estimates we assumed a geothermal gradient of $30\text{ }^{\circ}\text{C km}^{-1}$ starting from $1\text{ }^{\circ}\text{C}$ at the seafloor. However, the bulk resistivity depends more on porosity than temperature due to the exponent m in Archie's law. Furthermore, although lateral temperature variations in the oceanic basement are poorly constrained by observational data, we can probably rule out a thermal-only explanation for the resistivity decrease in the faulted crust since observations of anomalously low heat flow values suggest increased cooling from hydrothermal circulation along the fault planes (Grevemeyer et al., 2005), rather than the heating required to decrease resistivity. If indeed a significant temperature decrease accompanies the faulting, then our conversion of resistivity to porosity will underestimate the true porosity.

Fig. 7 shows the bulk porosity estimated from resistivity. On the oceanic plate the porosity decreases rapidly from the highly porous sediments to only a few percent throughout most of the crust, falling below one percent beneath the Moho. Bulk porosity in the bending fault region is up to a factor of two higher than the abyssal plain crust. The highest crustal porosities are observed on the margin slope.

Since the CSEM data sample bulk resistivity over spatial scales that include several fault damage zones and the unbroken matrix that separates them, the bulk porosity estimates given above using Archie's law provide a lower bound on what are likely to be significantly more porous fault damage zones. We can go further in the analysis if we represent the damage zones as conductive vertical sheets that are separated by a resistive matrix. The bulk resistivity ρ can be related to the damage zone resistivity ρ_f and the unbroken matrix resistivity ρ_m using the series conductivity law (e.g., Grant and West, 1965; Yu et al., 1997):

$$\frac{1}{\rho} = \frac{x}{\rho_f} + \frac{1-x}{\rho_m}, \quad (4)$$

where x is the volume fraction of the damage zone. We took the unfaulted abyssal plain resistivity to be representative of the unbroken matrix ρ_m and set ρ to be the average of all trench resistivity profiles, and then solved this equation for the damage zone resistivity ρ_f . We then applied Archie's law to ρ_f in order to estimate the damage zone porosity. Fig. 7 shows the resulting estimates for a range of volume fractions x .

The damage zone porosity estimates are significantly higher than the abyssal plain, but the extent of this increase depends on the volume fraction. In our simple parallel sheet fault model, the volume fraction is determined by the spacing between faults and the width of the damage zone. Ranero et al. (2003) found that the fault spacing varies from several kilometers on the outer rise to about 1 km near the base of the trench. In order to be detected by the reflection seismic data presented in Ranero et al. (2003), the fault damage zones must be at least a few tens of meters wide. A width of 40 m with 4 km spacing ($x=0.01$) could represent early faulting as plate bending initiates, whereas a width of 80 m spaced every 1 km ($x=0.08$) could be representative of the oldest, densest region of faulting at the base of the trench. Based on these values, the damage zone porosities in the lower crust span from about 1–20%, representing significantly porous channels for deep fluid circulation.

5. Discussion and conclusions

Our interpretation of the CSEM derived electrical resistivity and its implications for fluid circulation are shown in Fig. 8. The correlation between the bending faults at the outer rise and the concomitant decreases in crustal resistivity and mantle seismic velocity strongly suggests that the bending faults create the necessary permeable fluid pathways required for deeper alteration of the uppermost mantle. Since the CSEM model requires conductive pore fluids throughout the entire crust in order to explain the observed resistivity decrease, it is likely that fluids are also reaching the uppermost mantle via the fault damage zones. Any fluids reaching the mantle will lead to serpentinization. Therefore, the CSEM results suggest that the serpentinization is likely to explain the slow mantle seismic velocities rather than the alternative explanations of seismic anisotropy or fracture weakening (Ivandić et al., 2010; van Avendonk et al., 2011). There could be a combination of fracture weakening and serpentinization, but significant fracturing in the uppermost mantle would allow for deeper penetration of the observed crustal fluids and thus to mantle serpentinization.

Furthermore, since crustal porosity increases directly with the onset of the bending faults and persists at least until subduction, our results suggest that the time window for fluid input in the subducting plate is controlled by the width of the bending fault region and the rate of plate consumption at the trench. This time window may be the main factor controlling variations in slab hydration along the Middle America Trench. While many properties control the width of the faulted region, here the variable alignment between the seafloor spreading fabric and the trench axis is significant; offshore Nicaragua the alignment of the paleo spreading fabric and the trench axis is optimal for generating bending faults, whereas elsewhere along the Middle America Trench the spreading fabric is misaligned from the subduction direction by up to 25°, resulting in narrow and less pervasive bending fault regions (Ranero et al., 2005). The heavily faulted trench offshore Nicaragua allows for a longer time window for fluid penetration than possible in the narrower bending fault regions observed offshore Costa Rica and Guatemala (Ranero et al., 2005), providing an explanation for the anomalously high geochemical Ba/La ratios found in Nicaraguan arc lavas that indicate a strong slab fluid input (Carr et al., 2003; Rupke et al., 2002).

The upper plate on the margin slope is significantly less resistive than the oceanic plate and contains substantial lateral

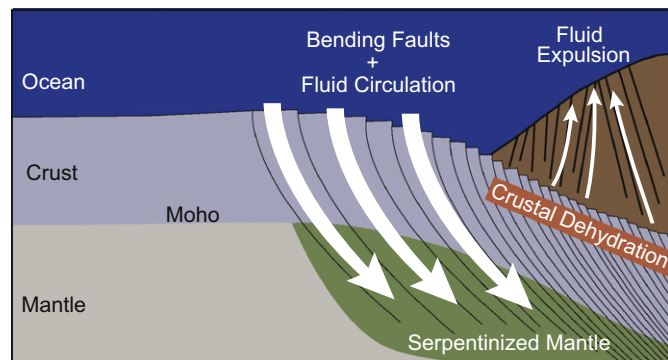


Fig. 8. Interpretation of observed electrical resistivity and seismically imaged bending faults. The incoming oceanic plate experiences extensional bending faults at the trench outer rise; these faults penetrate to mantle depths, creating highly permeable fault damage zones that allow for deep fluid circulation. Fluids reaching the mantle serpentinize peridotite in a region surrounding the faults. On the down going plate, sediment compaction and crustal dehydration reactions release fluids that percolate up through the highly fractured upper plate on the margin slope.

variations in the upper few kilometers. While these variations suggest a need for future 2D modeling efforts, we can make some general conclusions based on the 1D modeling used here. Considerable evidence suggests that the margin slope is dominated by subduction erosion processes, where material from the overriding plate is gradually eroded away from below (Ranero and von Huene, 2000). Dewatering of subducting sediments due to compaction and dehydration reactions is thought to lead to intense hydrofracturing and fluid expulsion on the continental slope (Ranero et al., 2008). Our observations of markedly higher porosities on the margin slope compared to the oceanic crust support the notion of a highly fractured upper plate (Fig. 7). Furthermore, numerous seafloor fluid seeps observed in a margin parallel band centered around 30 km landward of the trench (Sahling et al., 2008) coincide with the lowest crustal resistivities observed along the EM profile (Fig. 5a). This supports the hypothesis that a network of deep penetrating fractures allows fluids expelled by sediment dehydration on the deeper plate boundary to be focused through the overriding plate, rather than migrating back to the trench along the plate boundary (Sahling et al., 2008; Ranero et al., 2008).

Acknowledgments

This work was supported by National Science Foundation grants OCE-08411141 and OCE-0840894. We thank Murray Stein and the crew of the R/V Melville for ensuring a safe research cruise and the Governments of Nicaragua and Costa Rica for permission to work in their exclusive economic zones. The following people are thanked for their participation in the research cruise: Chris Armerding, Cambria Berger, Emily Carruthers, Ben Cohen, James Elsenbeck, Arnold Orange, Jake Perez, Keith Shadle, John Souders, Karen Weitemeyer, Brent Wheelock, Sam Zipper; Jacques Lemire and Arlene Jacobs, are thanked for their efforts with the cruise planning, mobilization and demobilization.

Appendix A. Supplementary data

Supplementary data associated with this article can be found in the online version at <http://dx.doi.org/10.1016/j.epsl.2012.07.020>.

References

- Abers, G.A., Plank, T., Hacker, B.R., 2003. The wet Nicaraguan slab. *Geophys. Res. Lett.* 30, 70-1–70-3.
- Alexander, R.T., Macdonald, K.C., 1996. Sea Beam, Sea MARC II, and ALVIN-based studies of faulting on the East Pacific Rise 920°–950°N. *Mar. Geophys. Res.* 18, 557–587.
- Archie, G., 1942. The electrical resistivity log as an aid in determining some reservoir characteristics. *Trans. Am. Inst. Mining Metall. Eng.* 146, 54–61.
- van Avendonk, H.J.A., Holbrook, W.S., Lizarralde, D., Denyer, P., 2011. Structure and serpentinization of the subducting Cocos plate offshore Nicaragua and Costa Rica. *Geochem. Geophys. Geosyst.* 12.
- Becker, K., 1985. Large-scale Electrical Resistivity and Bulk Porosity of the Oceanic Crust, Deep Sea Drilling Project Hole 504B, Costa Rica Rift. Initial rep of Deep Sea Drill Project.
- Becker, K., von Herzen, R.P., Francis, T.J.G., Anderson, R.N., Honnorez, J., Adamson, A.C., Alt, J.C., Emmermann, R., Kempton, P.D., Kinoshita, H., Laverne, C., Mottl, M.J., Newmark, R.L., 1982. In situ electrical resistivity and bulk porosity of the oceanic crust Costa Rica Rift. *Nature* 300, 594–598.
- Behrens, J.P., 2005. The Detection of Electrical Anisotropy in 35 Ma Pacific Lithosphere: Results from a Marine Controlled-Source Electromagnetic Survey and Implications for Hydration of the Upper Mantle. Ph.D. Thesis, University of California, San Diego.
- Brace, W.F., Orange, A.S., 1968. Further studies of effects of pressure on electrical resistivity of rocks. *J. Geophysical. Res. – Solid Earth* 73, 5407–5420.
- Carr, M., Feigenson, M., Patino, L., Walker, J., 2003. Volcanism and geochemistry in central America: progress and problems. In: Eiler, J. (Ed.), *Inside the Subduction Factory*. Geophysical Monograph. The American Geophysical Union, pp. 153–179.

- Constable, S., Cox, C.S., 1996. Marine controlled-source electromagnetic sounding. 2. The PEGASUS experiment. *J. Geophys. Res. – Solid Earth* 101, 5519–5530.
- Constable, S.C., Orange, A.S., Hoversten, G.M., Morrison, H.F., 1998. Marine magnetotellurics for petroleum exploration Part I: a sea-floor equipment system. *Geophysics* 63, 816–825.
- Constable, S.C., Parker, R.L., Constable, C.G., 1987. Occam's inversion – a practical algorithm for generating smooth models from electromagnetic sounding data. *Geophysics* 52, 289–300.
- Cox, C.S., 1981. On the electrical-conductivity of the oceanic lithosphere. *Phys. Earth Planet. Inter.* 25, 196–201.
- DeMets, C., 2001. A new estimate for present-day Cocos-Caribbean plate motion: implications for slip along the Central American volcanic arc. *Geophys. Res. Lett.* 28, 4043–4046.
- Everett, M.E., Constable, S., 1999. Electric dipole fields over an anisotropic seafloor: theory and application to the structure of 40 Ma Pacific Ocean lithosphere. *Geophys. J. Int.* 136, 41–56.
- Faccenda, M., Gerya, T.V., Burlini, L., 2009. Deep slab hydration induced by bending-related variations in tectonic pressure. *Nat. Geosci.* 2, 790–793.
- Grant, F.S., West, G.F., 1965. *Interpretation Theory in Applied Geophysics*. McGraw-Hill book.
- Grevemeyer, I., Kaul, N., Diaz-Naveas, J.L., Villinger, H.W., Ranero, C.R., Reichert, C., 2005. Heat flow and bending-related faulting at subduction trenches: case studies offshore of Nicaragua and Central Chile. *Earth Planet. Sci. Lett.* 236, 238–248.
- Grevemeyer, I., Ranero, C.R., Flueh, E.R., Klaeschen, D., Bialas, J., 2007. Passive and active seismological study of bending-related faulting and mantle serpentinization at the Middle America trench. *Earth Planet. Sci. Lett.* 258, 528–542.
- Ivandić, M., Grevemeyer, I., Berhorst, A., Flueh, E.R., McIntosh, K., 2008. Impact of bending related faulting on the seismic properties of the incoming oceanic plate offshore of Nicaragua. *J. Geophys. Res. – Solid Earth* 113, B05410.
- Ivandić, M., Grevemeyer, I., Bialas, J., Petersen, C.J., 2010. Serpentinization in the trench-outer rise region offshore of Nicaragua: constraints from seismic refraction and wide-angle data. *Geophys. J. Int.* 180, 1253–1264.
- Key, K., 2009. 1D inversion of multicomponent, multifrequency marine CSEM data: methodology and synthetic studies for resolving thin resistive layers. *Geophysics* 74, F9–F20.
- Key, K., 2012. Marine electromagnetic studies of seafloor resources and tectonics. *Surv. Geophys.* 33, 135–167.
- Key, K., Lockwood, A., 2010. Determining the orientation of marine CSEM receivers using orthogonal Procrustes rotation analysis. *Geophysics* 75, F63–F70.
- Key, K., Oval, J., 2011. A parallel goal-oriented adaptive finite element method for 2.5-D electromagnetic modelling. *Geophys. J. Int.* 186, 137–154.
- Masson, D.G., 1991. Fault patterns at outer trench walls. *Mar. Geophys. Res.* 13, 209–225.
- Myer, D., Constable, S., Key, K., 2011. Broad-band waveforms and robust processing for marine CSEM surveys. *Geophys. J. Int.* 184, 689–698.
- Parker, R., 1982. The existence of a region inaccessible to magneto-telluric sounding. *Geophys. J. R. Astron. Soc.* 68, 165–170.
- Peacock, S., 1990. Fluid processes in subduction zones. *Science*, 329–337.
- Ranero, C.R., Grevemeyer, I., Sahling, H., Barckhausen, U., Hensen, C., Wallmann, K., Weinrebe, W., Vannucchi, P., von Huene, R., McIntosh, K., 2008. Hydrogeological system of erosional convergent margins and its influence on tectonics and interplate seismogenesis. *Geochem. Geophys. Geosys.* 9, Q03S04.
- Ranero, C.R., von Huene, R., 2000. Subduction erosion along the Middle America convergent margin. *Nature* 404, 748–752.
- Ranero, C.R., Morgan, J.P., McIntosh, K., Reichert, C., 2003. Bending-related faulting and mantle serpentinization at the Middle America trench. *Nature* 425, 367–373.
- Ranero, C.R., Villasenor, A., Morgan, J.P., Weinrebe, W., 2005. Relationship between bend-faulting at trenches and intermediate-depth seismicity. *Geochem. Geophys. Geosys.* 6.
- Rupke, L., Morgan, J.P., Hort, M., Connolly, J., 2002. Are the regional variations in Central American arc lavas due to differing basaltic versus peridotitic slab sources of fluids? *Geology* 30, 1035–1038.
- Sahling, H., Masson, D.G., Ranero, C.R., Huhnerbach, V., Weinrebe, W., Klauke, I., Burk, D., Bruckmann, W., Suess, E., 2008. Fluid seepage at the continental margin offshore Costa Rica and southern Nicaragua. *Geochem. Geophys. Geosys.* 9, Q05S05.
- Shankland, T.J., Waff, H.S., 1974. Conductivity in fluid-bearing rocks. *J. Geophys. Res. – Solid Earth* 79, 4863–4868.
- Worzewski, T., Jegen, M., Kopp, H., Brasse, H., Castillo, W.T., 2010. Magnetotelluric image of the fluid cycle in the Costa Rican subduction zone. *Nat. Geosci.* 3, 1–4.
- Yu, L., Evans, R.L., Edwards, R.N., 1997. Transient electromagnetic responses in seafloor with triaxial anisotropy. *Geophys. J. Int.* 129, 292–304.